1 **Divergent changes in aerosol optical hygroscopicity and new particle**

2 **formation induced by heatwaves**

3

4 Yuhang Hao[1, a], Peizhao Li[1, a], Yafeng Gou[1], Zhenshuai Wang[1], Mi Tian[1], Yang Chen[2],

5 Ye Kuang[3], Hanbing Xu[4], Fenglian Wan[1], Yuqian Luo[1], Wei Huang[5], Jing Chen[1, 6, *]

6

7 [1] College of Environment and Ecology, Chongqing University, Chongqing 400045,

8 China

9 [2] Center for the Atmospheric Environment Research, Chongqing Institute of Green

10 and Intelligent Technology, Chinese Academy of Sciences, Chongqing 400714, China

11 [3] Institute for Environmental and Climate Research, Jinan University, Guangzhou

12 511443, China

13 [4] Experimental Teaching Center, Sun Yat-sen University, Guangzhou 510275, China

14 [5] National Meteorological Center, China Meteorological Administration, Beijing

15 100081, China

16 [6] Key Laboratory of Three Gorges Reservoir Region's Eco-Environment, Ministry of

17 Education, Chongqing University, Chongqing 400045, China

18

19 [a] These authors contributed equally

20

21 *Correspondence to*: Jing Chen (chen.jing@cqu.edu.cn)

Abstract. As a crucial climate-forcing driver, the aerosol optical enhancement factor (f(RH)) is significantly modulated by the evolution of particle number size distribution (PNSD), e.g., during new particle formation (NPF). The mechanisms regulating aerosol optical hygroscopicity during different NPF events and non-event days, particularly those influenced by heatwaves due to global warming, remain poorly understood. In the extremely hot summer of 2022 in urban Chongqing of southwest China, simultaneous measurements of aerosol optical and hygroscopic properties, PNSD, and bulk chemical compositions were conducted. Two distinct types of NPF were identified: the ones with relatively polluted period (P1) and clean cases during heatwave-dominated period (P2). Heatwaves triggered NPF earlier and prolonged the subsequent growth, resulting in smaller aerosol effective radius (R_{eff}) and lower growth rate. This agreed with the concurrently increased aerosol hemispheric backscattering fraction and scattering Ångström exponent. f(RH) was generally higher during NPF events in comparison to that for non-event cases in both periods. Heatwave-induced stronger photooxidation may intensify the formation of more hygroscopic secondary components, as well as the subsequent growth of pre-existing particles and newly formed ultrafine ones, thereby enhancing aerosol optical hygroscopicity especially during heatwave-influenced NPF events. The promoted f(RH) and lowered R_{eff} could synergistically elevate the aerosol direct radiative forcing, specifically under persistent heatwave conditions. Further in-depth exploration on molecular-level characterizations and aerosol radiative impacts of both direct and indirect interactions during weather extremes (e.g., heatwaves) with the warming climate are recommended.

1 Introduction

Weather extremes (e.g., heatwaves) have become more and more frequent and intense largely due to the global climate change, and the heatwave-driven environmental, climatic, and health effects have garnered widespread attention

50 (Hauser et al., 2016; Sun et al., 2016). The China Climate Bulletin 2022 confirmed

51 that the national average temperature reached an unprecedented high level since 2012

52 (China Meteorological Administration, 2022), and the risk of heatwaves in China will

53 persist and potentially intensify in the future (Guo et al., 2016; Li et al., 2017).

54 Extreme heatwave events could pose significant threats to human health, the survival

55 of organisms, agriculture, and socio-economic activities (e.g., power supply

56 restrictions) (Anderson and Bell, 2011; Ma et al., 2021; Su, 2021). Moreover,

57 heatwaves can trigger natural disasters such as droughts and wildfires, affecting social

58 stability (Sharma and Mujumdar, 2017).

59   Heatwaves could also affect the atmospheric physical and chemical processes by

60 modulating ambient meteorological conditions. Specifically, extremely high

61 temperature weather is typically characterized by a combination of intensified solar

62 radiation with elevated temperature and low humidity levels. This could significantly

63 affect the formation and evolution of secondary aerosols in the atmosphere (Bousiotis

64 et al., 2021; Hamed et al., 2011; Kurtén et al., 2007), given that the air temperature is

65 crucial for chemical reactions (Xu et al., 2011). New particle formation (NPF) serves

66 as a crucial source of atmospheric particulate matter and plays a significant role in the

67 secondary transformation processes in the atmosphere (Zhu et al., 2021). Generally,

68 NPF involves the initial formation of thermodynamically stable clusters from

69 condensable vapors (e.g., ammonia, sulfuric acid, and organic precursor gases) and

70 subsequent growth of the formed clusters, eventually reaching detectable sizes or even

71 larger dimensions (Kerminen et al., 2018; Kulmala et al., 2003, 2012). Over time,

72 these newly formed particles have the potential to serve as cloud condensation nuclei

73 (CCN), thereby impacting the global climate (Salma et al., 2016). NPF events

74 normally introduce a sharp increase in the number concentration of nucleation mode

75 particles within a short time, altering the particle number size distribution (PNSD).

76 These variations in PNSD likely influence intrinsic physicochemical properties of

77 aerosols, such as the optical hygroscopicity (Chen et al., 2014; Titos et al., 2016; Zhao

78 et al., 2019).

79   Aerosol hygroscopicity plays a critical role in the atmospheric environment and

80   climate change, given the complex interaction between aerosol particles and water

81   vapor (Zhao et al., 2019; Zieger et al., 2011). Water uptake by aerosols not only alters

82   the particle size and composition (e.g., as reflected in the aerosol refractive index) but

83   also impacts aerosol scattering efficiency, which further contributes to the uncertainty

84   in aerosol radiative forcing estimation (Titos et al., 2016, 2021). The aerosol optical

85   hygroscopicity parameter, f(RH), defined as the ratio of the scattering coefficient at a

86   certain RH to that of the dry condition, was widely used to describe the aerosol

87   scattering enhancement through water uptake (Covert et al., 1972; Titos et al., 2016;

88   Zhao et al., 2019). Numerous studies have demonstrated that f(RH) is influenced by

89   the size distribution, in addition to particle chemical composition (Chen et al., 2014;

90   Kuang et al., 2017; Petters and Kreidenweis, 2007; Quinn et al., 2005). NPF could

91   alter the size distribution thereby aerosol optical properties, nonetheless, there is

92   currently limited research on the impact of NPF on aerosol optical hygroscopicity (Ma

93   et al., 2016; Ren et al., 2021). It is suggested that the influence of NPF on aerosol

94   hygroscopicity was likely due to changes in aerosol chemical composition at different

95   stages of NPF events (Cheung et al., 2020), whereas the subsequent particle growth

96   associated with NPF events can significantly affect particle hygroscopicity as well

97   (Wu et al., 2016). Although there have been a great many studies on chemical

98   composition dependences of aerosol hygroscopicity (e.g., the variation in composition

99   of precursor species during NPF events), it is important to acknowledge that the

100   utilized chemical compositions of NPF were either from $PM_{2.5}$ or PM_1 bulk data,

101   which may differ from the corresponding composition of newly formed ultrafine

102   particles primarily in the nucleation and Aitken modes. This may further introduce

103   bias in exploring the impacts of NPF events on aerosol optical hygroscopicity if solely

104   based on $PM_{2.5}$ chemical composition, especially in the initial nucleation stage of NPF.

105   Hence, more comprehensive investigations on the influencing mechanisms of aerosol

106   optical hygroscopicity from different perspectives are required, e.g., for the aspects of

107   the evolution of particle size distribution in modulating aerosol optical and

108   hygroscopic properties (Tang et al., 2019; Zhao et al., 2019). Additionally, field

109   observations on f(RH) under extreme weather conditions (e.g., heatwaves) are rather

110   scarce, largely hindering our understanding of how weather extremes (e.g., extremely

111   high temperature) influence the optical hygroscopic properties of aerosols. This

112   knowledge gap further impedes comprehensive understanding of the aerosol water

113   uptake property and resulted effects on air quality and the climate under varied

114   synoptic conditions.

115   During the summer of 2022, a rare heatwave event raged throughout the

116   Sichuan-Chongqing region of southwest China, with the daily maximum temperature

117   exceeding 40 °C lasted for 29 days observed at Beibei meteorological station in

118   Chongqing (Hao et al., 2023). This persistent heatwave not only impacted residents'

119   daily lives significantly, but also affected the aerosol optical and hygroscopic

120   properties likely through NPF and relevant atmospheric processing during the period.

121   In this study, a field observation was conducted by using a combination of a

122   home-built humidified nephelometer system and a scanning mobility particle sizer

123   (SMPS), along with the total suspended particle (TSP) filter sampling. A main goal of

124   this study is to investigate the influence of heatwaves on NPF events and subsequent

125   impacts on aerosol optical and hygroscopic properties. Furthermore, we aimed to

126   explore the mechanisms behind the variability in f(RH) under different meteorological

127   conditions and NPF events. This study will further enrich insights into the potential

128   environmental and climatic impacts due to variations in the aerosol optical

129   hygroscopicity and size distribution, specifically under weather extremes (e.g.,

130   heatwaves) with the changing climate.

131

2 Data and Methods

2.1 Field observation

134   A continuous field observation on aerosol optical, hygroscopic and chemical

135   properties was carried out from July 29 to August 19, 2022. The detailed description

136   of the observation site is available in Supporting Information, S1. During the

137   observation period, urban Chongqing suffered a rare heatwave (Fig. S1), which

138   significantly affected the local transportation and industrial activities (Hao et al.,

139   2023). Based on the temperature records and concurrent aerosol light scattering data,

140   the whole study period was categorized into two stages: (1) the normally hot period

141   (with the daily maximum temperature seldomly above 35°C) from 29 July to 6 August

142   (simply labeled as P1); (2) the heatwave-dominated cleaner period (persistent

143   occurrence of the hourly temperature over 40°C, and the hourly total scattering

144   coefficient at 525 nm below 100 Mm^{-1}) during 7-19 August 2022 (marked as P2).

145   **2.2 Instrumentation and methods**

146   **2.2.1 Measurements of aerosol optical hygroscopicity**

147   The humidified nephelometer system, consisting of two three-wavelength (i.e.,

148   450, 525, and 635 nm) nephelometers (Model Aurora 3000, Ecotech Inc.) and a

149   humidification unit, was used to determine the aerosol light scattering enhancement

150   factor, f(RH). Briefly, the aerosol scattering ($\sigma_{sca, \lambda}$) and backscattering coefficients

151   ($\sigma_{bsca, \lambda}$) were detected in a dry state (RH <30%) and at a fixed RH level of 85% ± 1%,

152   respectively, with the humidification efficiency regulated automatically by a

153   temperature-controlled water bath.

154   Hence, f(RH) could be calculated as the ratio of the aerosol scattering coefficient

155   at a predefined RH ($\sigma_{sca, RH}$) to the dry ($\sigma_{sca, dry}$) state, i.e., f(RH) = $\sigma_{sca, RH}$ / $\sigma_{sca, dry}$

156   (Covert et al., 1972). In this study, the f(RH) discussed is mainly targeted for the 525

157   nm wavelength, unless otherwise specified. More information about the measurement

158   of humidified nephelometer system was illustrated in S2 of the supplement.

159   In additional to f(RH), aerosol optical parameters, such as scattering Ångström

160   exponent (SAE; Schuster et al., 2006) and hemispheric backscattering fraction (HBF;

161   Collaud Coen et al., 2007), were calculated as below:

162
$$SAE_{\lambda 1/\lambda 2} = \frac{-\ln(\sigma_{sca, \lambda 1}/\sigma_{sca, \lambda 2})}{\ln(\lambda 1/\lambda 2)} \qquad (1)$$

163
$$HBF_\lambda = \frac{\sigma_{bsca, \lambda}}{\sigma_{sca, \lambda}} \qquad (2)$$

164   where $\sigma_{sca,\ \lambda}$ and $\sigma_{bsca,\ \lambda}$ represent the aerosol scattering and backscattering

165   coefficients at a specific wavelength λ (e.g., $\lambda 1$, $\lambda 2$), respectively.

166   Both HBF and SAE reflect crucial optical properties of aerosols, e.g., an elevated

167   HBF (or SAE) generally signifies a higher concentration (or a smaller particle size) of

168   fine particles within the aerosol population (Jefferson et al., 2017; Kuang et al., 2017;

169   Luoman et al., 2019). The HBF and SAE discussed in this study are targeted for the

170   dry condition, unless otherwise specified. Based on the measurements with the

171   humidified nephelometer system, the equivalent aerosol liquid water content (ALWC)

172   and the corresponding fraction of ALWC (f_W) can also be obtained (Kuang et al, 2018;

173   see S2 of the supplement).

174   The SMPS-measured concurrent particle number size distributions were further

175   utilized to calculate the aerosol effective radius (R_{eff}) and representative parameters

176   for NPF events, e.g., the growth rate (GR) of new particle, condensation sink (CS)

177   and coagulation sink (CoagS) (Kulmala et al., 2012). More details are provided in the

178   supplement.

179

2.2 Determination of the aerosol direct radiative forcing (ADRF) enhancement
180
181   **factor**

182   Given the high sensitivity of aerosol optical properties (e.g., f(RH)) to the

183   changes in RH under real atmospheric conditions, the influence of RH, or rather the

184   aerosol hygroscopicity, on ADRF can be quantitatively estimated with the radiative

185   transfer model by the following equation (Chylek and Wong, 1995; Kotchenruther et

186   al., 1999; L. Zhang et al., 2015):

187    $$\Delta F_R(RH) = -(S_0 / 4) \times [T_a^2 \times (1 - A_C)] \times [2 \times (1 - R_s)^2 \times \beta(RH) \times \tau_s - 4 \times R_s \times \tau_a] \quad (3)$$

188   where S_0 is the solar constant, T_a is the atmosphere transmittance, A_C is the

189   fractional cloud amount, R_s is the albedo of the underlying surface, $\beta(RH)$ is the

190   upscattering fraction at a defined RH, τ_s and τ_a are the optical thicknesses of the

191   aerosol layer due to light scattering and light absorption, respectively, which can be

192   expressed as follows (Kotchenruther et al., 1999):

193
$$\tau_s = M \times \alpha_s \times f(RH), \tau_a = M \times \alpha_a \qquad (4)$$

194   where M is the column burden of aerosol (unit: gm^{-2}), α_s is the mass scattering

195   efficiency (MSE), and α_a is the mass absorption efficiency (MAE). The direct

196   radiative forcing is usually calculated with the assumption that the absorption

197   enhancement is negligible, in comparison to the aerosol scattering enhancement (Xia

198   et al., 2023).

199   Hence, the dependence of ADRF on RH (i.e., $f_{RF}(RH)$) can be estimated by

200   equation (5) (Chylek and Wong, 1995; Kotchenruther et al., 1999; L. Zhang et al.,

201   2015):

202
$$f_{RF}(RH) = \frac{\Delta F_R(RH)}{\Delta F_R(dry)} = \frac{(1-R_s)^2 \times \beta(RH) \times \alpha_s \times f(RH) - 2 \times R_s \times \alpha_a}{(1-R_s)^2 \times \beta(dry) \times \alpha_s \times f(dry) - 2 \times R_s \times \alpha_a} \qquad (5)$$

203   where the constant parameters used were R_s = 0.15, α_a = 0.3 $m^2 \cdot g^{-1}$ (Hand and

204   Malm, 2007; Fierz-Schmidhauser et al., 2010). It should be noted that the assumed

205   constant α_a might introduce some uncertainty in the calculated $f_{RF}(RH)$, given the fact

206   that the contribution of absorption by brown carbon was unknown, although the mass

207   fraction of BC in TSP remained almost constant (i.e., 4.6% ± 1.1%, Fig. S2) during

208   the observation period. The parameter α_s was calculated by dividing $\sigma_{sca, 525}$ in the dry

209   condition by the mass concentration of PM$_{2.5}$ (i.e., $\alpha_s = \sigma_{sca, 525}$ / PM$_{2.5}$). β could be

210   calculated empirically from the measured HBF: β = 0.0817 + 1.8495 × HBF − 2.9682

211   × HBF^2 (Delene and Ogren, 2002).

212   Results of the offline chemical analysis with TSP filter samples are provided in

213   S3. Given that the particle number and mass size distributions of components such as

214   sulfate and organics from diverse emission sources were primarily concentrated

215   within the submicron size range (An et al., 2024), the bulk chemical compositions of

216   TSP could provide a reasonably good reference for the characterization of NPF and

217   related optical and hygroscopic properties of PM$_{2.5}$. It should be noted that the

218   corresponding mass fraction of some components (e.g., crustal materials) likely

219   biased for larger particles. The simultaneous meteorological and air quality data can

220   be found in S4.

3 Results and discussion

3.1 Overview of the aerosol optical hygroscopicity and PNSD measurements

Figure. 1 displayed the time series of the measured aerosol scattering coefficients, f(RH), PNSD, and the corresponding meteorological conditions and air pollutants during the study period. A sharp decrease in aerosol scattering coefficients and $PM_{2.5}$, accompanied with the continuous excellent visibility over 20 km was observed after August 6, indicating a markedly cleaner environment during P2 in comparison to P1 in summer 2022 of Chongqing. This could be largely attributed to the reduction in anthropogenic emissions (e.g., NO_2, CO) from limited outdoor activities influenced by the heatwaves in P2, as well as partly suspended industries and transportation to alleviate the power shortage issue. Notably, the increased wind speed and enhanced mixing layer height (MLH) also enabled a more favorable atmospheric diffusion condition in P2, facilitating the dilution of surface air pollutants (Zhang et al., 2008). However, a higher mass concentration of SO_2 was observed in the P2 period, likely due to a surge in electricity demand and resulted higher emissions from power plants operating almost at full capacity during the heatwave (Su, 2021; Teng et al., 2022). Moreover, significant discrepancies in the aerosol optical and hygroscopic properties were observed under different synoptic conditions (Table S2). Both HBF and SAE were higher during the P2 period, aligning with the smaller R_{eff} (Table S2). The f(RH) was found to be larger in heatwave days, with the mean values of 1.6 ± 0.1 and 1.7 ± 0.2 during the P1 and P2 periods, respectively. Differently, ALWC was more abundant during the normally hot P1 period than the heatwave-dominated P2 period, likely due to that the derivation algorithm of ALWC utilized in this study (Kuang et al., 2018) was partly dependent on (e.g., positively correlated) the aerosol scattering coefficient in the dry condition. The mean $\sigma_{sca,\ 525}$ for P2 was about 46.8% of that for the P1 period, and the corresponding mean level of ALWC was approximately 55.8% of that for P1. This partly agrees with the stronger aerosol optical hygroscopicity with a marginally higher f_W during the P2 period, highlighting a complex interaction between the optical enhancement and aerosol physicochemical properties.

250   The particle number size distribution data suggested that NPF events appeared in

251   about half the number of observation days (Fig. 1i), with the frequency during the P2

252   period (53.8%) slightly higher than that of P1 (44.4%). This suggests the rather

253   frequent summer NPF events in Chongqing, notably higher than those observed in

254   other regions of the world, e.g., Beijing (16.7%, Deng et al., 2020; ~20%, Wang et al.,

255   2013), Dongguan (4%, Tao et al., 2023), Hyytiälä (<40%, Dada et al., 2017) and

256   LiLLE (<20%, Crumeyrolle et al., 2023). Moreover, the frequent NPF events during

257   heatwaves formed substantially ultrafine particles that are of less contribution to

258   aerosol optical properties in comparison to large particles, partially explaining the

259   significantly lower levels of total scattering coefficients observed during the P2

260   period.
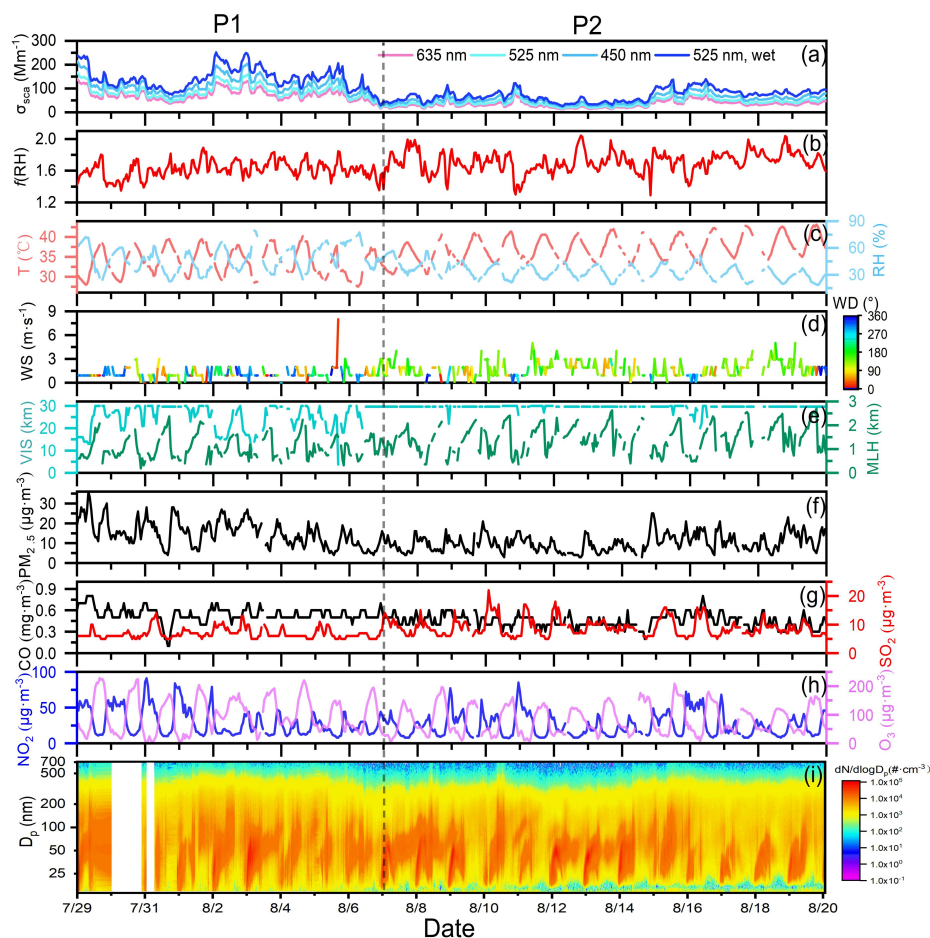
Figure 1. Time series of the measured aerosol scattering coefficients, f(RH), meteorological conditions, air pollutants, and particle number size distribution during the study period.

3.2 Characteristics of NPF events in different periods

Aside from gaseous precursors (e.g., SO_2, volatile organic compounds), meteorological conditions also play a key role in the occurrence of NPF events. In brief, NPF events are more likely to appear under sunny and clean conditions (Bousiotis et al., 2021; Crumeyrolle et al., 2023; Deng et al., 2021; Wang et al., 2017). To further explore the characteristics of NPF events in different periods, the

time-averaged diurnal variations of meteorological parameters and air pollutant

concentrations during both NPF events and non-event days are presented in Fig. 2.
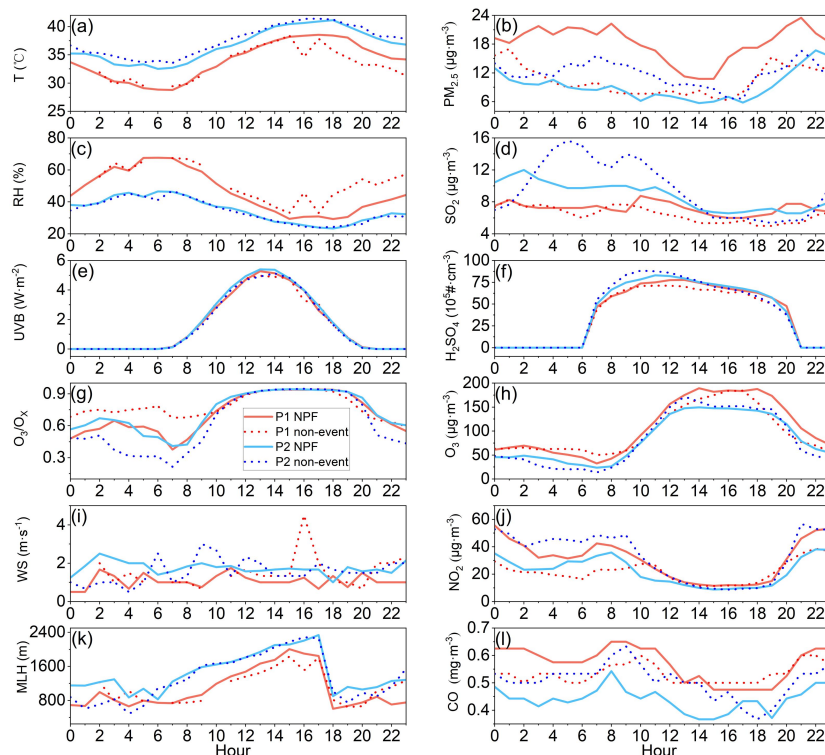
Figure 2. Diurnal variations of temperature **(a)**, $PM_{2.5}$ mass loading **(b)**, RH **(c)**, SO_2 **(d)**, UVB **(e)**, H_2SO_4 **(f)**, O_3/O_X **(g)**, O_3 **(h)**, WS **(i)**, NO_2 **(j)**, MLH **(k)** and CO **(l)** during P1 (red) and P2 (blue) NPF events (solid line), as well as the corresponding non-event days (dash line).

NPF events during the P1 period tended to occur in relatively polluted environments compared to that of P2 NPF events, as evidenced by the higher $\sigma_{sca, 525}$, increased air pollutant concentrations and lower visibility levels during P1 (Table S2, Fig. 1). On P2 NPF event days, the overall mean $\sigma_{sca, 525}$ was 33.2 ± 11.7 Mm^{-1}, decreased by 68.0% (39.3%) in comparison to that for P1 NPF event days (P2 non-event days). In addition, the mean $PM_{2.5}$ concentration was even lower than 10.0 $\mu g \cdot m^{-3}$, and the corresponding visibility level was almost reaching the upper detection limit of 30 km. All the above implies that the P2 NPF events were generally

286 accompanied with a much cleaner environment. It is notable that the increase in SO_2

287 concentration after 9:00 (Fig. 2d), along with the significant decrease in $PM_{2.5}$ mass

288 loadings thereby lowered CS or CoagS after 8:00 during P1 NPF events (Fig. 2b),

289 likely favored the occurrence of NPF events. The higher gas-phase sulfuric acid (i.e.,

290 H_2SO_4, as estimated with the UVB and SO_2 concentration, Lu et al., 2019, S4) on the

291 same NPF event days (Fig. 2f), further suggesting that sulfuric acid concentration was

292 a critical factor for the occurrence of P1 NPF events.

293 Meanwhile, the diurnal evolutions of meteorological conditions (e.g., T, RH,

294 MLH) for NPF events were distinct between P1 and P2 periods, although relatively

295 insignificant differences were observed for both NPF events and non-event days

296 within a same period (Fig. 2). This might suggest that meteorological factors might

297 not be the predominant determining factor of NPF occurrence, while NPF could be

298 accompanied with quite different meteorological conditions depending on gaseous

299 precursors and preexisting condensation sinks. For instance, the heatwave-influenced

300 NPF events were typically of clean-type NPF, characterized with lower background

301 aerosol loading, higher temperature and favorable atmospheric dispersion capacity

302 with the higher MLH. However, it is reported that excessive heat can increase the

303 evaporation rate of critical acid-base clusters during the nucleation process and reduce

304 the stability of initial molecular clusters (Bousiotis et al., 2021; Kurtén et al., 2007;

305 Zhang et al., 2012). On the other hand, the emission rate of biogenic VOCs (BVOCs,

306 e.g., isoprene, monoterpene) from nearby plants and trees would decrease when

307 temperature exceeded around 40 °C (Guenther et al., 1993; Pierce and Waldruff,

308 1991), despite that BVOCs plays a key role in the nucleation mechanism of NPF

309 (Wang et al., 2017; Zhang et al., 2004). Hence, the even higher temperature (e.g.,

310 T >40 °C) likely hindered the occurrence and subsequent growth of NPF during

311 non-event days of the P2 period, in spite of higher concentrations of SO_2 and H_2SO_4.

312 To further investigate the effect of heatwave on NPF events, the diurnal

313 variations of aerosol number and volume concentrations, as well as R_{eff}, for different

314 modes were illustrated in Fig. S4, and the relationship between temperature and the

315 duration of NPF events was displayed in Fig. S5. The NPF events influenced by

316 heatwaves usually initiated earlier (Fig. S5), with the number concentration of

317 nucleation mode particles ($N_{Nuc.}$) in P2 NPF cases peaked about an hour earlier (whilst

318 relatively lower) in comparison to P1 event days (Fig. S4a). This implies that

319 heatwaves may accelerate the attainment of the temperature threshold of NPF events,

320 as evidenced by the earlier NPF start time corresponding to higher temperature ranges

321 (Fig. S5). Furthermore, the end time of subsequent particle growth during P2 period

322 was even later (i.e., ~ 21:00 LT) than that of P1 cases (Fig. S5). Given the lower GR

323 during P2 NPF events (Table S2), these explosively formed new particles could

324 persist longer in the warmer atmosphere and probably undergo aging processes with a

325 relatively higher oxidation degree. This is supported by the commonly higher ratios of

326 secondary organic carbon (SOC) to organic carbon (OC) (i.e., SOC/OC >0.5) during

327 the P2 NPF event days (Fig. S2b). The diurnal patterns of aerosol volume

328 concentrations for different size modes were similar to that of aerosol number

329 concentrations during NPF events (Fig. S4b1-b3). It is worth noting that both the R_{eff}

330 of Aitken mode particles ($R_{Ait.}$) and accumulation mode particles ($R_{Acc.}$) were smaller

331 during P2 NPF events than that of P1 NPF events (Fig. S4c2-c3), which may further

332 influence size-dependent aerosol optical and hygroscopic properties (e.g., $\sigma_{sca, 525}$,

333 HBF, SAE, f(RH)). The decrease in $R_{Ait.}$ and $R_{Acc.}$ during heatwaves could be

334 attributed to three factors: (1) evaporation of the outer layer of particles due to

335 extremely high temperature (Bousiotis et al., 2021; Cusack et al., 2013; Deng et al.,

336 2020; Li et al., 2019); (2) lower GR of particles under a cleaner environment; (3)

337 reduced emissions of larger primary particles during the P2 period.

338 **3.3 Characteristics of the aerosol optical and hygroscopic properties during NPF**
339 **events**

340 Diurnal variations of the aerosol optical and hygroscopic parameters during NPF

341 events were shown in Fig. 3, and the corresponding results for non-event days can

342 refer to Fig. S6. Generally, $\sigma_{sca, 525}$ possessed a similar bimodal diurnal pattern to that

343 of the accumulation mode aerosol volume concentration ($V_{Acc.}$) (Fig. S4b3), as

344 supported by the positive correlation between $\sigma_{sca, 525}$ and SMPS-measured aerosol

345 volume concentration (Fig. S8). This is also consistent with the Mie theory, with a

346 stronger increase in the scattering efficiency for accumulation mode particles (Titos et

347 al., 2021). The diurnal pattern of $\sigma_{sca,\,525}$ also varied distinctly between different NPF

348 events. Specifically, a minor peak of $\sigma_{sca,\,525}$ around 12:00 (Fig. 3a) was influenced by

349 the newly formed particles during P2 NPF events, which contributed more

350 significantly to the aerosol number and volume concentrations within 100 nm size

351 ranges in pretty clean environments (Fig. S3c, g). Instead of a noontime peak, $\sigma_{sca,\,525}$

352 was observed with an early peak around the morning rush hours and a maximum

353 value similarly occurred at the nighttime on P1 NPF event days.
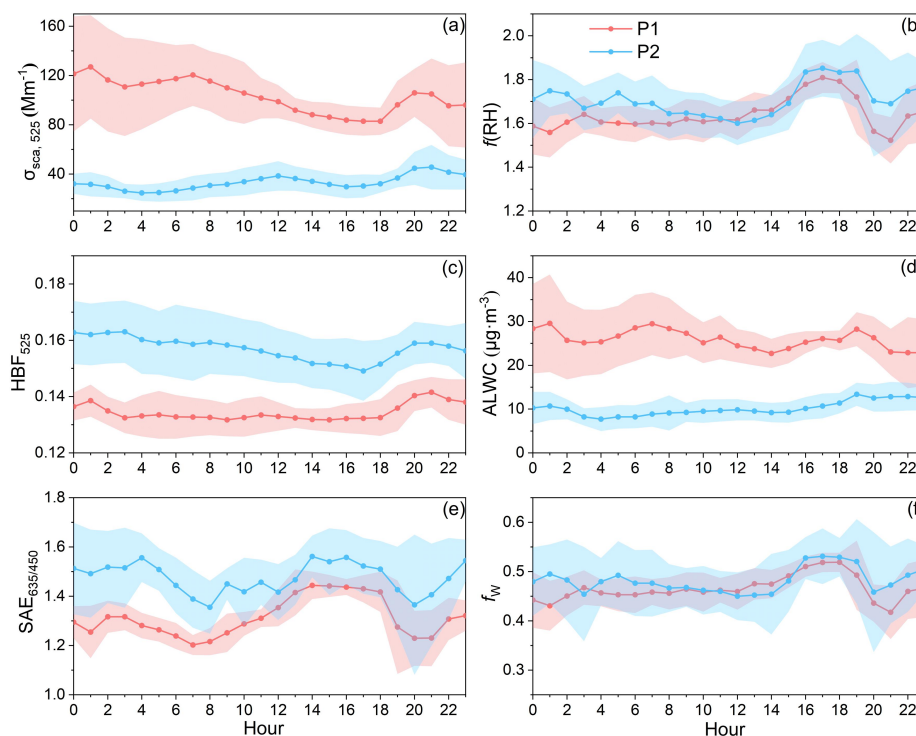
354

Figure 3. Diurnal variations of $\sigma_{sca,\,525}$ **(a)**, f(RH) **(b)**, HBF_{525} **(c)**, ALWC **(d)**,

SAE$_{635/450}$ **(e)** and f_W **(f)** on NPF event days during P1 (red line) and P2 (blue line)

periods. The shaded areas stand for the corresponding $\pm 1\sigma$ standard deviations.

358 Both HBF and SAE during P2 NPF events were significantly higher than that

359 of P1 NPF cases (Fig. 3c, e), largely due to the smaller R$_{eff}$ during P2

360 heatwave-dominated NPF events (Table S2). Moreover, the correlation between HBF

361   (or SAE) and particle size in each mode was relatively weaker on NPF event days

362   than on non-event days, especially for P2 NPF events (Fig. S10). A strongest negative

363   correlation was found between HBF and R_{eff} of the accumulation mode in comparison

364   to other modes, highlighting that HBF is more sensitive to the size distribution of

365   accumulation mode particles (Collaud Coen et al., 2007). Given that NPF would

366   largely enhance the abundance of both nucleation and Aitken mode aerosols, no

367   significant variation in HBF was observed during the daytime due to the weakened

368   correlation between HBF and $R_{Acc.}$ of NPF events. SAE is commonly used as an

369   indicator of particle size distribution, almost decreasing monotonously with the

370   increase of aerosol size within 1 μm (Kuang et al., 2017, 2018; Luoma et al., 2019).

371   Accordingly, SAE decreased over the morning and evening rush hours when coarse

372   particles (e.g., aged particles, road dust, automobile exhaust) generated during

373   anthropogenic activities, accompanied with an increase in CO that is taken as the

374   proxy for primary emissions (Fig. 2l) (Yarragunta et al., 2020). On the contrary, the

375   abundant ultrafine particles formed during NPF events led to a continuous increase in

376   SAE during the day.

377   f(RH) exhibited a similar diurnal pattern on the P1 and P2 NPF event days

378   (Fig. 3b). During the daytime, f(RH) remained relatively stable and gradually

379   increased until peaking around 16:00-18:00, with a generally higher f(RH)

380   particularly after 15:00 during P2 NPF events than that of P1 cases. The insignificant

381   fluctuation of relatively lower f(RH) levels before the noon could be attributed to the

382   continuous development of the mixing layer (Fig. 2k), leading to an efficient mixing

383   of particles in the nocturnal residual layer with anthropogenic emissions near the

384   ground. Additionally, photochemical reactions in the afternoon facilitated the

385   formation of more hygroscopic secondary aerosols with a higher oxidation level (Liu

386   et al., 2014; R. Zhang et al., 2015). The diurnal patterns of O_3 and the O_3/O_X ratio (i.e.,

387   an indicator of atmospheric oxidation capacity, where $O_X = O_3 + NO_2$, Tian et al.,

388   2021) also showed similar trends (Fig. 2g, 2h). The presence of black carbon (BC)

389   mixed with organic compounds (e.g., from traffic emissions and residential cooking

390   activities) explained the rapid decrease in f(RH) during the evening rush hours (Liu et

391 al., 2011). Furthermore, the daily mean f(RH) during NPF events was higher than that

392 of non-event days (Table S2), particularly after the ending of NPF events around

393 12:00. Given that newly formed particles were too small to significantly impact the

394 total light scattering (Fig. S7), this indicates that the atmospheric conditions

395 conducive to the occurrence of NPF may promote further growth (e.g., via

396 photooxidation or atmospheric aging processes) of pre-existing particles and newly

397 formed ones, leading to enhanced aerosol optical hygroscopicity as clued from the

398 concurrent variations of ALWC and f_W in urban Chongqing during hot summer (Asmi

399 et al., 2010; Wang et al., 2019; Wu et al., 2016). The diurnal pattern of ALWC closely

400 mirrored the variation in $\sigma_{sca, 525}$, while f_W followed the similar evolution of f(RH).

401 This suggests that ALWC was more sensitive to changes in the aerosol volume

402 concentration, as determined by the corresponding retrieval algorithm (Kuang et al.,

403 2018). The relatively higher f_W levels (e.g., even exceeded 50% sometimes) verified

404 the enhancement of aerosol hygroscopicity during NPF events in comparison to that
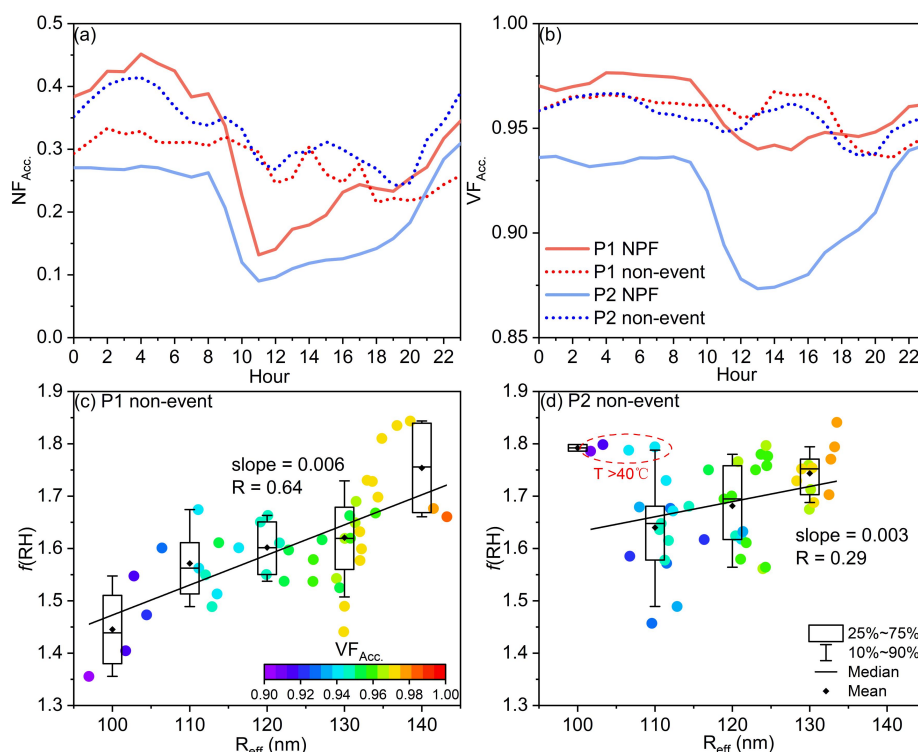
405 of non-event days.

3.4 Heatwave-induced divergent changes in aerosol optical hygroscopicity

407 To further explore the impacts of heatwaves on f(RH) during diverse NPF events,

408 data mainly within the time window of 08:00-22:00 (i.e., typically covered the

409 complete process of NPF and subsequent growth, while excluded higher RH

410 conditions at night) were utilized for the following discussion.

411 A positive correlation between f(RH), R_{eff} and the volume fraction of

412 accumulation mode particles (VF$_{Acc.}$) was found on non-event days (Fig. 4c-d), when

413 the aerosol size distribution was undisturbed by newly formed ultrafine particles and

414 the corresponding VF$_{Acc.}$ maintained around a relatively high level of 0.95 (Fig. 4a-b).

415 The notably positive correlation between f(RH) and R_{eff} could be linked to the

416 secondary formation of hygroscopic particles within the accumulation mode,

417 primarily via photochemical reactions and further intensified by heatwaves during the

418 day particularly of the P2 period (Gu et al., 2023; Liu et al., 2014; R. Zhang et al.,

419 2015; Zhang et al., 2024). Consequently, f(RH) at a specific R_{eff} was generally higher

420   during the P2 period in comparison to that of P1 (Fig. 4c-d), also with high f(RH)

421   levels observed for smaller size cases of R_{eff} <110 nm under some extremely high

422   temperature conditions (T >40 °C, as highlighted by the red dashed circle in Fig. 4d).

423   The higher SOC/OC on P2 non-event days further demonstrated the stronger

424   secondary aerosol formation in comparison to P1 non-event days (Fig. S2b).

425

Figure 4. Diurnal variations of **(a)** the number fraction ($NF_{Acc.}$) and **(b)** volume

fraction of accumulation mode particles ($VF_{Acc.}$) on P1 (red) and P2 (blue) NPF event

days (solid line), as well as non-event days (dash line). The relationship of f(RH) with

R_{eff} and $VF_{Acc.}$ (as indicated by the colored dots) on P1 **(c)** and P2 non-event days **(d)**

during the 08:00-22:00 time window.

431   Nevertheless, f(RH) was almost independent of the two parameters (i.e., R_{eff}

432   and $VF_{Acc.}$) for NPF events (Fig. S11a1-a2). This is mainly due to the explosive

433   formation of ultrafine particles during NPF events, significantly altering aerosol size

434   distributions and inducing large fluctuations in the number and volume fractions of

435   accumulation mode particles (Fig. 4a-b). Therefore, characterizing f(RH) with the

436   corresponding R_{eff} of aerosol populations was no longer applicable. Alternatively,

437   SAE was commonly used to estimate or parameterize f(RH) (Titos et al., 2014; Xia et

438   al., 2023; Xue et al., 2022), in line with the similar diurnal patterns of f(RH) and SAE

439   observed in this study. Figure 5 demonstrated a significantly positive correlation

440   between f(RH) and SAE during NPF events, with a similar slope of approximately

441   0.65 suggesting the consistent variation of f(RH) with SAE across both periods. As

442   larger particles contributed higher to the aerosol volume concentrations (Fig. S3), the

443   decrease of SAE also corresponded to an increase in $\sigma_{sca,\ 525}$ (Fig. 5a2, b2). In this

444   sense, f(RH) increased with SAE whereas decreased with $\sigma_{sca,\ 525}$, or rather the

445   pollution level during NPF events. Meanwhile, the cleaner environment of P2 period

446   generally possessed a lower CS (Table S2, as denoted by the size of circles in Fig. 5),

447   thereby in favor of the occurrence of NPF event. Such a positive (negative)

448   correlation of f(RH) with SAE (CS) was more pronounced in heatwave-induced high

449   temperature days during P2 period. The possible reasons can be attributed to the

450   following two aspects. One is related to the relatively smaller aerosol R_{eff} (with a

451   larger SAE) due to the lower GR, likely influenced by the evaporation of

452   newly-formed unstable clusters and particle coatings under heatwaves (Bousiotis et al.,

453   2021; Cusack et al., 2013; Deng et al., 2020) during the subsequent growth of aerosols.

454   Secondly, the higher temperature was normally associated with stronger

455   photochemical oxidation, which could intensify the formation of secondary aerosol

456   components with a higher hygroscopicity (Asmi et al., 2010; Gu et al., 2023; Liu et al.,

457   2014; Wu et al., 2016; R. Zhang et al., 2015; Zhang et al., 2024). This is further

458   supported by the relatively higher levels of UVB (P1: 2.6 ± 1.9 W·m^{-2} versus P2: 2.7

459   ± 2.0 W·m^{-2}) and O_3/O_X (P1: 0.81 ± 0.17 versus P2: 0.82 ± 0.17) during P2 heatwave

460   days, also in line with a recent study which demonstrated that heatwaves affected

461   secondary organic aerosols (SOA) formation and aging by accelerating

462   photooxidation in Beijing (Zhang et al., 2024).

463   It is worth noting that f(RH) did not show a consistently higher level after the

464   NPF occurrence during P2 period, and it was slightly higher within the first few hours

465   of NPF occurrence during P1 NPF events (Fig. 3b). In fact, aerosol optical

466   hygroscopicity not fully corresponds to the bulk hygroscopicity primarily determined

467   by aerosol chemical components, and the variability in aerosol optical features also

468   plays a key role in f(RH). In this sense, the size-dependency of aerosol optical

469   properties should be considered. The size-resolved $\sigma_{sca,\ 525}$ distribution and

470   size-resolved cumulative frequency distribution (CFD) of $\sigma_{sca,\ 525}$ over different NPF

471   events were calculated using the Mie theory, with good agreements between the

472   theoretically calculated and measured $\sigma_{sca,\ 525}$ values (R^2 = 0.99). As shown in Fig. S7

473   and Fig. S9, new particles must grow into the accumulation mode size at least before

474   they can exert a significant influence on the total scattering coefficient. The critical

475   sizes corresponding to the cumulative frequency of 50% in $\sigma_{sca,\ 525}$ were 358.7 nm and

476   333.8 nm on P1 and P2 NPF event days, respectively. This indicates that relatively

477   smaller particles contributed a slightly higher portion to $\sigma_{sca,\ 525}$ during P2 NPF events,

478   while the $\sigma_{sca,\ 525}$ of P1 NPF events was mainly contributed by larger particles.

479   Nevertheless, the Mie theory suggests that these smaller particles generally have a

480   weaker enhancement in total scattering after hygroscopic growth, in comparison to

481   larger size particles (Collaud Coen et al., 2007, Fig. S7). Consequently, the changes in

482   aerosol optical and hygroscopic properties necessitate consideration of both aerosol

483   optical and chemical characteristics during different NPF events. The contribution of

484   newly formed ultrafine particles to aerosol optical properties was insignificant within

485   the first few hours of NPF occurrence, leading to a reduced enhancement in aerosol

486   light scattering as characterized by a smaller R_{eff} during P2 NPF events in comparison

487   to P1 NPF events. In contrast, the growth of pre-existing and newly formed particles

488   into larger sizes would subsequently affect bulk aerosol optical properties, which was

489   evidenced by the enhancement in aerosol extinction coefficient observed after NPF

490   occurrence in a recent study (Sun et al., 2024). Specifically, particles could undergo a

491   longer and more intensified photochemical aging process during P2 NPF events as

492   influenced by persistent heatwaves, which facilitated the secondary formation of

493   hygroscopic aerosols and resulted in a higher f(RH) after 15:00 (Fig. 3b).
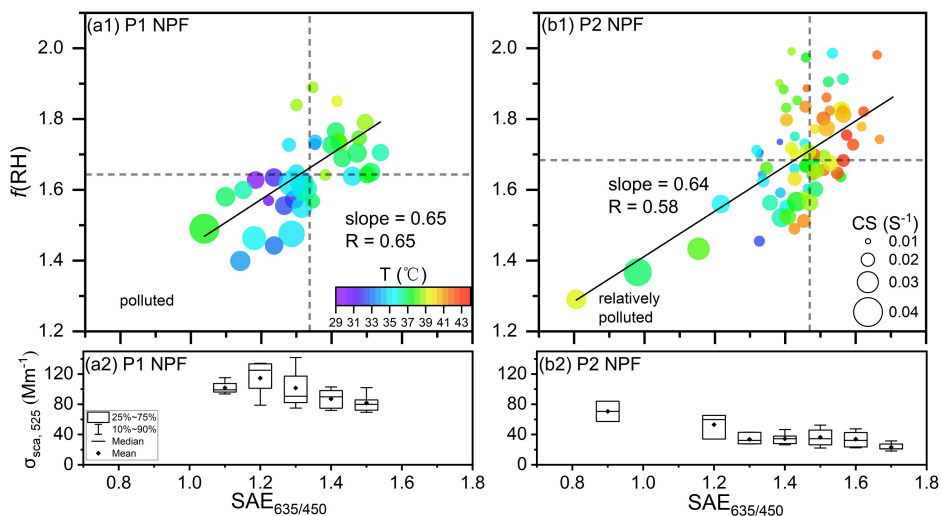
Figure 5. (a1) The relationship between f(RH) and $SAE_{635/450}$, as well as temperature (as indicated by the color of dots) and CS (as denoted by the size of circles), on P1 NPF event days during the 08:00-22:00 time window. The vertical (horizontal) dash line represents the median value of $SAE_{635/450}$ (f(RH)). **(a2)** The corresponding $\sigma_{sca,\ 525}$ under different $SAE_{635/450}$ levels on P1 NPF event days. **(b1-b2)** The same but for P2 NPF event days.

3.5 f(RH)-induced changes in aerosol direct radiative forcing

501

502   The changes in f(RH) have significant implications for aerosol direct radiative

503   forcing. Despite considerably lower $\sigma_{sca, 525}$ results during heatwaves, the

504   corresponding mean f_{RF}(RH) levels particularly for P2 NPF event days were higher

505   than that of the P1 cases (Fig. 6a). A robust positive correlation ($R^2 = 0.68$) was

506   observed between f(RH) and aerosol radiative forcing enhancement factor, f_{RF}(RH)

507   (Fig. 6b). This is likely attributed to the enhanced f_{RF}(RH) with the larger forward

508   scattering ratio β, or rather higher HBF for smaller particle sizes, as supported by a

509   generally negative correlation between f_{RF}(RH) and R_{eff}. Specifically, the highest

510   f_{RF}(RH) value of 2.2 ± 0.2 was observed on P2 NPF event days, characterized with the

511   highest f(RH) and smallest R_{eff} (i.e., highest HBF) of the entire study period.

512   The definition of f_{RF}(RH) in Eq.(5) implies the dependences of f_{RF}(RH) on both

513   f(RH) and HBF-derived β(RH) and β(dry), or rather the ratio of $HBF_{525, RH}/HBF_{525}$.

514   The mean $HBF_{525, RH}$ was generally larger than HBF_{525} in this study, specifically with

515   the $HBF_{525, RH}/HBF_{525}$ ratios centered around 1.8 and even approached 2.5 on P2 NPF

516   event days (Fig. 6c, Table S2). This could be different from the classical Mie theory

517   with the spherical-particle premise, i.e., the observed light backscattering was

518   enhanced after hydration likely resulted from the evolution in particle morphology

519   that significantly influences their optical properties (Mishchenko 2009). The

520   organic-rich particles might remain non-spherical even after water uptake due to the

521   efficient evaporation of organic coatings under extremely hot weather conditions, as

522   evidenced by a recent study that high temperature and RH conditions could accelerate

523   the evaporation rate of SOA (Li et al., 2019). Meanwhile, the backward scattering

524   intensity of non-spherical particles is suggested to be much larger than its spherical

525   counterparts at scattering angles between 90° and 150° (Mishchenko 2009; Yang et al.,

526   2007). Furthermore, ultrafine particles would significantly contribute to both total

527   light scattering and backscattering coefficients (Fig. S7) after hygroscopic growth, if

528   the aerosol population was large enough (e.g., during NPF processes). These

529   combined effects could potentially change particle morphology and optical properties

530   (e.g., elevated the $HBF_{525, RH}$) particularly during heatwave-influenced NPF events,

531   characterized with the smallest aerosol R_{eff} (102.8 ± 12.4 nm), lowest number fraction

532   of accumulation mode particles (0.20 ± 0.10), and a higher SOC/OC ratio. The higher

533    $HBF_{525, RH}/HBF_{525}$ ratios increased the HBF-derived $\beta(RH)/\beta(dry)$ levels, in

534   combination of the elevated $f(RH)$, further resulting in the highest $f_{RF}(RH)$ observed

535   during P2 NPF events. Given that previously observed $HBF_{525, RH}$ was typically lower

536   than HBF_{525} (Titos et al., 2021; Xia et al., 2023; L. Zhang et al., 2015), the mean

537    $f_{RF}(RH)$ results of this study ($f_{RF}(85\%) = 2.0 \pm 0.2$) were significantly higher than

538   those observed in the Yangtze River Delta ($f_{RF}(85\%) = 1.5$, L. Zhang et al., 2015), the

539   North China Plain ($f_{RF}(80\%) = 1.6 \pm 0.2$, Xia et al., 2023), and some other regions in

540   the world (Titos et al., 2021, Fig. 6d). It should be noted that the reported $f_{RF}(RH)$ for

541   the UGR site (Spain) was even higher, likely due to the relatively larger HBF in that

542   area (Titos et al., 2014; 2021).

543
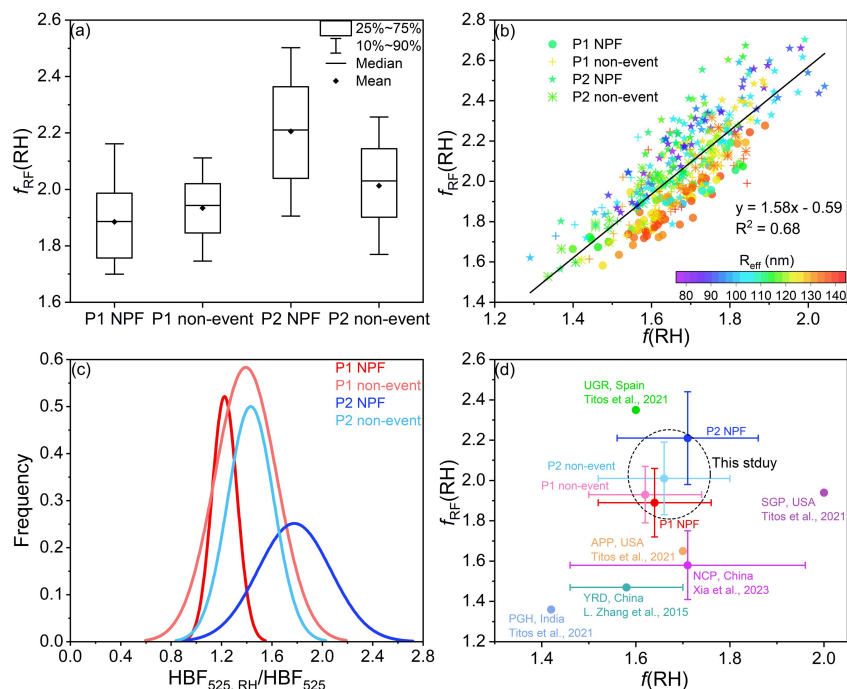
Figure 6. (a) The box-plot of $f_{RF}(RH)$ during P1 or P2 NPF event and non-event days.

(b) The relationship between $f_{RF}(RH)$ and $f(RH)$, as colored by the corresponding R_{eff},

during P1 or P2 NPF event and non-event days (shown in different symbols). **(c)**

547   Occurrence frequency of the ratio $HBF_{525, RH}/HBF_{525}$ during P1 or P2 NPF event and

548   non-event days. **(d)** The mean $f_{RF}(RH)$ under different $f(RH)$ levels (the error bars

549   stand for ± one standard deviations corresponding to $f_{RF}(RH)$ and $f(RH)$, respectively),

550   along with the reported $f_{RF}(RH)$ and $f(RH)$ data for other regions in the world.

551   A recent study has indicated that continuous reduction of $PM_{2.5}$ mass loadings

552   can increase the net solar radiation, thereby promoting NPF events (Zhao et al., 2021).

553   Given the complexity and dynamic evolution of the atmospheric environment, these

554   can further alter the intrinsic properties of aerosol particles (e.g., $f(RH)$, HBF,

555   morphology), potentially feeding back into aerosol-radiation interactions. Our

556   findings suggest that NPF and growth events may elevate aerosol optical

557   hygroscopicity in rather hot environments, e.g., the Basin area and tropical regions.

558   Meanwhile, NPF serves as a crucial secondary transformation process in the

559   atmosphere (Zhu et al., 2021). The favorable atmospheric diffusion capability ensured

560   the mixing of newly formed particles into the upper boundary layer, where is colder

561   and more humid than that near the surface during heatwaves (Jin et al., 2022). Hence,

562   the enhancement of aerosol optical hygroscopicity during the subsequent growth of

563   pre-existing and newly formed particles possibly exacerbates secondary pollution and

564   even triggers haze events (Hao et al., 2024; Kulmala et al., 2021). On the other hand,

565   the new particles of higher hygroscopicity could contribute more to the activation of

566   CCN, thereby modulating the aerosol-cloud interactions and further the global climate

567   (Ren et al., 2021; Sun et al., 2024; Wu et al., 2015). Additionally, the simultaneous

568   decrease in aerosol effective radius and possibly evaporation-induced non-spherical

569   particle morphology further enhance the aerosol direct radiative forcing enhancement

570   factor, potentially amplifying the cooling effect mainly caused by light scattering

571   aerosols. This highlights the needs for further in-depth exploration on aerosol

572   radiative impacts at weather extremes (e.g., heatwaves) with the changing climate,

573   given the continuous reductions of anthropogenic emissions and more intense

574   emissions of biogenic origins with the global warming. Besides, more detailed

575   information on the evolution of particle morphology with the changing environment

576   (e.g., varied temperature and RH) would enrich insights into the aerosol radiative

577   forcing.

578

4 Conclusions and implications

580   NPF events frequently occurred in urban Chongqing of southwest China in the

581   summer of 2022, accompanied with continuous heatwaves. Concurrent measurements

582   of aerosol optical and hygroscopic properties, PNSD, and bulk chemical compositions

583   were conducted to elucidate the mechanisms behind the variations in aerosol optical

584   hygroscopicity during different NPF event and non-event days.

585   NPF events exhibited distinct characteristics during the normally hot (P1,

586   relatively polluted) and heatwaves-dominated (P2, quite clean) periods. NPF within

587   P1 period was favored by the decrease in background aerosol loading and the higher

588   abundance of H_2SO_4. NPF events that occurred during the heatwave P2 period were

589   characterized with relatively lower CS, CoagS, and GR, as well as a smaller R_{eff}, than

590   P1 NPF cases. In comparison to the P1 NPF events, heatwaves initiated NPF earlier

591   and prolonged the subsequent growth during P2, likely intensifying the photochemical

592   oxidation due to heatwave-induced aging processes and modulating the evolution of

593   aerosol size distributions differently.

594   Heatwaves also significantly influenced the aerosol optical and hygroscopic

595   properties. Distinct diurnal patterns of $\sigma_{sca,\ 525}$ were observed for different types of

596   NPF events, with a minor $\sigma_{sca,\ 525}$ noontime peak occurred in P2 instead of peaked

597   earlier around the morning rush hours on P1 NPF event days. HBF and SAE were

598   significantly higher on P2 NPF event days, primarily due to the relatively smaller R_{eff}

599   for heatwave-influenced NPF cases. f(RH) remained relatively stable during the

600   daytime of NPF event days and peaked around 16:00-18:00, likely due to the

601   intensive photochemical reactions and accordingly enhanced formation of more

602   hygroscopic secondary aerosols. These secondary components could be more

603   abundant due to heatwave-induced stronger photooxidation, further resulting in a

604   higher f(RH) particularly during the subsequent growth of pre-existing particles and

605 newly formed ultrafine ones during P2 NPF events in comparison to that of P1 NPF

606 cases.

607   Compared with non-event cases, the generally higher levels of daily mean f(RH)

608 suggested that the aerosol optical hygroscopicity was enhanced during NPF events in

609 hot summer of urban Chongqing. A significantly positive (negative) correlation

610 between f(RH) and SAE (CS, $\sigma_{sca, 525}$, or rather the pollution level) was observed for

611 both periods, with a more pronounced correlation during heatwave-influenced NPF

612 events. The aerosol light scattering or volume concentration was mainly contributed

613 by the larger accumulation-mode particles, while more ultrafine particles dominated

614 the size distribution especially for the initial stage of heatwave-influenced NPF events,

615 further leading to a diminished aerosol scattering enhancement capability in

616 comparison to P1 NPF events.

617   Changes in f(RH) have significant implications for the aerosol direct radiative

618 forcing. A robust positive (negative) correlation existed between f_{RF}(RH) and f(RH)

619 (R_{eff}). Despite a lower $\sigma_{sca, 525}$ during heatwaves, the corresponding mean f_{RF}(RH) was

620 relatively higher and the maximum value of 2.2 ± 0.2 was observed on P2 NPF event

621 days, associated with the highest f(RH) (1.7 ± 0.2), smallest R_{eff} (102.8 ± 12.4 nm),

622 and highest $HBF_{525, RH}/HBF_{525}$ ratios (1.8 ± 0.3). The above highlights that heatwaves

623 could influence the NPF and atmospheric processing (although with a decreased

624 aerosol effective radius likely due to evaporation-resulted non-spherical particle

625 morphology under persistently high temperature conditions), thereby enhancing

626 aerosol optical hygroscopic growth and potentially reducing the net solar radiation

627 directly especially in hot summer. Further explorations on detailed molecular

628 characterizations and aerosol radiative impacts including the aerosol-cloud

629 interactions of weather extremes (e.g., heatwaves) with the changing climate are

630 highly recommended.

631

632 **Data availability.** Data will be available upon request.

633

References

An, J., Lu, Y., Huang, D. D., Ding, X., Hu, Q., Yan, R., Qiao, L., Zhou, M., Huang, C., Wang, H., Fu, Q., Yu, F., and Wang, L.: Sectoral Size - Resolved Particle Number Emissions With Speciation: Emission Profile - Based Quantification and a Case Study in the Yangtze River Delta Region, China, J. Geophys. Res. Atmos., 1–22, https://doi.org/10.1029/2024JD041234, 2024.

Asmi, E., Frey, A., Virkkula, A., Ehn, M., Manninen, H. E., Timonen, H., Tolonen-Kivimäki, O., Aurela, M., Hillamo, R., and Kulmala, M.: Hygroscopicity and chemical composition of antarctic sub-micrometre aerosol particles and observations

659   of new particle formation, Atmos. Chem. Phys., 10, 4253–4271,

660   https://doi.org/10.5194/acp-10-4253-2010, 2010.

661   Bousiotis, D., Brean, J., Pope, F. D., Dall'Osto, M., Querol, X., Alastuey, A., Perez,

662   N., Petäjä, T., Massling, A., Klenø Nøjgaard, J., Nordstrøm, C., Kouvarakis, G.,

663   Vratolis, S., Eleftheriadis, K., Niemi, J. V., Portin, H., Wiedensohler, A., Weinhold,

664   K., Merkel, M., Tuch, T., and Harrison, R. M.: The effect of meteorological

665   conditions and atmospheric composition in the occurrence and development of new

666   particle formation (NPF) events in Europe, Atmos. Chem. Phys., 21, 3345–3370,

667   https://doi.org/10.5194/acp-21-3345-2021, 2021.

668   Brooke Anderson, G. and Bell, M. L.: Heat waves in the United States: Mortality risk

669   during heat waves and effect modification by heat wave characteristics in 43 U.S.

670   communities, Environ. Health Perspect., 119, 210–218,

671   https://doi.org/10.1289/ehp.1002313, 2011.

672   Chen, J., Zhao, C. S., Ma, N., and Yan, P.: Aerosol hygroscopicity parameter derived

673   from the light scattering enhancement factor measurements in the North China Plain,

674   Atmos. Chem. Phys., 14, 8105–8118, https://doi.org/10.5194/acp-14-8105-2014,

675   2014.

676   China Meteorological Administration, 2022. China Climate Bulletin 2022.

677   https://www.cma.gov.cn/zfxxgk/gknr/qxbg/202303/t20230324_5396394.html.

678   Accessed on 23 March 2023. (in Chinese).

679   Cho Cheung, H., Chung-Kuang Chou, C., Siu Lan Lee, C., Kuo, W. C., and Chang, S.

680   C.: Hygroscopic properties and cloud condensation nuclei activity of atmospheric

681   aerosols under the influences of Asian continental outflow and new particle formation

682   at a coastal site in eastern Asia, Atmos. Chem. Phys., 20, 5911–5922,

683   https://doi.org/10.5194/acp-20-5911-2020, 2020.

684   Chylek, P. and Wong, J.: Effect of absorbing aerosols on global radiation budget,

685   Geophys. Res. Lett., 22, 929–931, https://doi.org/10.1029/95GL00800, 1995.

686   Collaud Coen, M., Weingartner, E., Nyeki, S., Cozic, J., Henning, S., Verheggen, B.,

687   Gehrig, R., and Baltensperger, U.: Long-term trend analysis of aerosol variables at the

688   high-alpine   site   Jungfraujoch,   J.   Geophys.   Res.   Atmos.,   112,

689   https://doi.org/10.1029/2006JD007995, 2007.

690   Covert, D. S., Charlson, R. J., and Ahlquist, N. C.: A Study of the Relationship of

691   Chemical Composition and Humidity to Light Scattering by Aerosols, J. Appl.

692   Meteorol.,   11,   968–976,

693   https://doi.org/10.1175/1520-0450(1972)011<0968:asotro>2.0.co;2, 1972.

694   Crumeyrolle, S., Kontkanen, J. S. S., Rose, C., Velazquez Garcia, A., Bourrianne, E.,

695   Catalfamo, M., Riffault, V., Tison, E., Ferreira De Brito, J., Visez, N., Ferlay, N.,

696   Auriol, F., and Chiapello, I.: Measurement report: Atmospheric new particle

697   formation at a peri-urban site in Lille, northern France, Atmos. Chem. Phys., 23,

698   183–201, https://doi.org/10.5194/acp-23-183-2023, 2023.

699   Cusack, M., Alastuey, A., and Querol, X.: Case studies of new particle formation and

700   evaporation processes in the western Mediterranean regional background, Atmos.

701   Environ., 81, 651–659, https://doi.org/10.1016/j.atmosenv.2013.09.025, 2013.

702   Dada, L., Paasonen, P., Nieminen, T., Buenrostro Mazon, S., Kontkanen, J., Peräkylä,

703   O., Lehtipalo, K., Hussein, T., Petäjä, T., Kerminen, V. M., Bäck, J., and Kulmala, M.:

704   Long-term analysis of clear-sky new particle formation events and nonevents in

705   Hyytiälä,   Atmos.   Chem.   Phys.,   17,   6227–6241,

706   https://doi.org/10.5194/acp-17-6227-2017, 2017.

707   Dal Maso, M., Kulmala, M., Riipinen, I., Wagner, R., Hussein, T., Aalto, P. P., and

708   Lehtinen, K. E. J.: Formation and growth of fresh atmospheric aerosols: Eight years

709   of aerosol size distribution data from SMEAR II, Hyytiälä, Finland, Boreal Environ.

710   Res., 10, 323–336, 2005.

711   Delene, D. J. and Ogren, J. A.: Variability of aerosol optical properties at four North

712   American surface monitoring sites, J. Atmos. Sci., 59, 1135–1150,

713   https://doi.org/10.1175/1520-0469(2002)059<1135:VOAOPA>2.0.CO;2, 2002.

714   Deng, C., Cai, R., Yan, C., Zheng, J., and Jiang, J.: Formation and growth of sub-3

715   nm particles in megacities: Impact of background aerosols, Faraday Discuss., 226,

716   348–363, https://doi.org/10.1039/d0fd00083c, 2021.

717   Deng, C., Fu, Y., Dada, L., Yan, C., Cai, R., Yang, D., Zhou, Y., Yin, R., Lu, Y., Li,

718   X., Qiao, X., Fan, X., Nie, W., Kontkanen, J., Kangasluoma, J., Chu, B., Ding, A.,

719   Kerminen, V. M., Paasonen, P., Worsnop, D. R., Bianchi, F., Liu, Y., Zheng, J., Wang,

720   L., Kulmala, M., and Jiang, J.: Seasonal characteristics of new particle formation and

721   growth in urban Beijing, Environ. Sci. Technol., 54, 8547–8557,

722   https://doi.org/10.1021/acs.est.0c00808, 2020.

723   Fierz-Schmidhauser, R., Zieger, P., Gysel, M., Kammermann, L., Decarlo, P. F.,

724   Baltensperger, U., and Weingartner, E.: Measured and predicted aerosol light

725   scattering enhancement factors at the high alpine site Jungfraujoch, Atmos. Chem.

726   Phys, 10, 2319–2333, 2010.

727   Gu, Y., Huang, R. J., Duan, J., Xu, W., Lin, C., Zhong, H., Wang, Y., Ni, H., Liu, Q.,

728   Xu, R., Wang, L., and Li, Y. J.: Multiple pathways for the formation of secondary

729   organic aerosol in the North China Plain in summer, Atmos. Chem. Phys., 23,

730   5419–5433, https://doi.org/10.5194/acp-23-5419-2023, 2023.

731   Guenther, A. B., Monson, R. K., and Fall, R.: Isoprene and monoterpene emission

732   rate variability: Observations with eucalyptus and emission rate algorithm

733   development, J. Geophys. Res. Atmos., 96, 10799–10808,

734   https://doi.org/10.1029/91jd00960, 1991.

735   Guo, X., Huang, J., Luo, Y., Zhao, Z., and Xu, Y.: Projection of heat waves over
736   China for eight different global warming targets using 12 CMIP5 models, Theor. Appl.
737   Climatol., 128, 507–522, https://doi.org/10.1007/s00704-015-1718-1, 2016.

738   Hamed, A., Korhonen, H., Sihto, S. L., Joutsensaari, J., Jrvinen, H., Petäjä, T., Arnold,
739   F., Nieminen, T., Kulmala, M., Smith, J. N., Lehtinen, K. E. J., and Laaksonen, A.:
740   The role of relative humidity in continental new particle formation, J. Geophys. Res.
741   Atmos., 116, 1–12, https://doi.org/10.1029/2010JD014186, 2011.

742   Hand, J. L. and Malm, W. C.: Review of aerosol mass scattering efficiencies from
743   ground-based measurements since 1990, J. Geophys. Res. Atmos., 112,
744   https://doi.org/10.1029/2007JD008484, 2007.

745   Hao, Y., Gou, Y., Wang, Z., Huang, W., Wan, F., Tian, M., and Chen, J.: Current
746   challenges in the visibility improvement of urban Chongqing in Southwest China:
747   From the perspective of PM2.5-bound water uptake property over 2015–2021, Atmos.
748   Res., 300, 107215, https://doi.org/10.1016/j.atmosres.2023.107215, 2024.

749   Hao, Z., Chen, Y., Feng, S., Liao, Z., An, N., and Li, P.: The 2022
750   Sichuan-Chongqing spatio-temporally compound extremes: a bitter taste of novel
751   hazards, Sci. Bull., 68, 1337–1339, https://doi.org/10.1016/j.scib.2023.05.034, 2023.

752   Hauser, M., Orth, R., and Seneviratne, S. I.: Role of soil moisture versus recent
753   climate change for the 2010 heat wave in western Russia, Geophys. Res. Lett., 43,
754   2819–2826, https://doi.org/10.1002/2016GL068036, 2016.

755   Jefferson, A., Hageman, D., Morrow, H., Mei, F., and Watson, T.: Seven years of
756   aerosol scattering hygroscopic growth measurements from SGP: Factors influencing
757   water   uptake,   J.   Geophys.   Res.   Atmos.,   122,   9451–9466,
758   https://doi.org/10.1002/2017JD026804, 2017.

759   Jin, X., Li, Z., Wu, T., Wang, Y., Cheng, Y., Su, T., Wei, J., Ren, R., Wu, H., Li, S.,
760   Zhang, D., and Cribb, M.: The different sensitivities of aerosol optical properties to

761 particle concentration, humidity, and hygroscopicity between the surface level and the

762 upper boundary layer in Guangzhou, China, Sci. Total Environ., 803, 150010,

763 https://doi.org/10.1016/j.scitotenv.2021.150010, 2022.

764 Kerminen, V. M., Chen, X., Vakkari, V., Petäjä, T., Kulmala, M., and Bianchi, F.:

765 Atmospheric new particle formation and growth: Review of field observations,

766 Environ. Res. Lett., 13, https://doi.org/10.1088/1748-9326/aadf3c, 2018.

767 Kotchenruther, R. A., Hobbs, P. V., and Hegg, D. A.: Humidification factors for

768 atmospheric aerosols off the mid-Atlantic coast of the United States, J. Geophys. Res.

769 Atmos., 104, 2239–2251, https://doi.org/10.1029/98JD01751, 1999.

770 Kuang, Y., He, Y., Xu, W., Zhao, P., Cheng, Y., Zhao, G., Tao, J., Ma, N., Su, H.,

771 Zhang, Y., Sun, J., Cheng, P., Yang, W., Zhang, S., Wu, C., Sun, Y., and Zhao, C.:

772 Distinct diurnal variation in organic aerosol hygroscopicity and its relationship with

773 oxygenated organic aerosol, Atmos. Chem. Phys., 20, 865–880,

774 https://doi.org/10.5194/acp-20-865-2020, 2020.

775 Kuang, Y., Zhao, C. S., Zhao, G., Tao, J. C., Xu, W., Ma, N., and Bian, Y. X.: A

776 novel method for calculating ambient aerosol liquid water content based on

777 measurements of a humidified nephelometer system, Atmos. Meas. Tech., 11,

778 2967–2982, https://doi.org/10.5194/amt-11-2967-2018, 2018.

779 Kuang, Y., Zhao, C., Tao, J., Bian, Y., Ma, N., and Zhao, G.: A novel method for

780 deriving the aerosol hygroscopicity parameter based only on measurements from a

781 humidified nephelometer system, Atmos. Chem. Phys., 17, 6651–6662,

782 https://doi.org/10.5194/acp-17-6651-2017, 2017.

783 Kulmala, M., Dada, L., Daellenbach, K. R., Yan, C., Stolzenburg, D., Kontkanen, J.,

784 Ezhova, E., Hakala, S., Tuovinen, S., Kokkonen, T. V., Kurppa, M., Cai, R., Zhou, Y.,

785 Yin, R., Baalbaki, R., Chan, T., Chu, B., Deng, C., Fu, Y., Ge, M., He, H., Heikkinen,

786 L., Junninen, H., Liu, Y., Lu, Y., Nie, W., Rusanen, A., Vakkari, V., Wang, Y., Yang, G.,

787 Yao, L., Zheng, J., Kujansuu, J., Kangasluoma, J., Petaja, T., Paasonen, P., Jarvi, L.,

788 Worsnop, D., Ding, A., Liu, Y., Wang, L., Jiang, J., Bianchi, F., and Kerminen, V. M.:

789 Is reducing new particle formation a plausible solution to mitigate particulate air

790 pollution in Beijing and other Chinese megacities?, Faraday Discuss., 226, 334–347,

791 https://doi.org/10.1039/d0fd00078g, 2021.

792 Kulmala, M., Petäjä, T., Nieminen, T., Sipilä, M., Manninen, H. E., Lehtipalo, K., Dal

793 Maso, M., Aalto, P. P., Junninen, H., Paasonen, P., Riipinen, I., Lehtinen, K. E. J.,

794 Laaksonen, A., and Kerminen, V. M.: Measurement of the nucleation of atmospheric

795 aerosol particles, Nat. Protoc., 7, 1651–1667, https://doi.org/10.1038/nprot.2012.091,

796 2012.

797 Kulmala, M.: How Particles Nucleate and Grow, Science, 302, 1000–1001,

798 https://doi.org/10.1126/science.1090848, 2003.

799 Kurtén, T., Torpo, L., Ding, C. G., Vehkamäki, H., Sundberg, M. R., Laasonen, K.,

800 and Kulmala, M.: A density functional study on water-sulfuric acid-ammonia clusters

801 and implications for atmospheric cluster formation, J. Geophys. Res. Atmos., 112, 1–7,

802 https://doi.org/10.1029/2006JD007391, 2007.

803 Li, Y., Ding, Y., and Li, W.: Observed trends in various aspects of compound heat

804 waves across China from 1961 to 2015, J. Meteorol. Res., 31, 455–467,

805 https://doi.org/10.1007/s13351-017-6150-2, 2017.

806 Li, Z., Tikkanen, O. P., Buchholz, A., Hao, L., Kari, E., Yli-Juuti, T., and Virtanen, A.:

807 Effect of Decreased Temperature on the Evaporation of α-Pinene Secondary Organic

808 Aerosol Particles, ACS Earth Sp. Chem., 3, 2775–2785,

809 https://doi.org/10.1021/acsearthspacechem.9b00240, 2019.

810 Liu, H. J., Zhao, C. S., Nekat, B., Ma, N., Wiedensohler, A., Van Pinxteren, D.,

811 Spindler, G., Müller, K., and Herrmann, H.: Aerosol hygroscopicity derived from

812 size-segregated chemical composition and its parameterization in the North China

813   Plain, Atmos. Chem. Phys., 14, 2525–2539, https://doi.org/10.5194/acp-14-2525-2014,

814   2014.

815   Liu, P. F., Zhao, C. S., Göbel, T., Hallbauer, E., Nowak, A., Ran, L., Xu, W. Y., Deng,

816   Z. Z., Ma, N., Mildenberger, K., Henning, S., Stratmann, F., and Wiedensohler, A.:

817   Hygroscopic properties of aerosol particles at high relative humidity and their diurnal

818   variations in the north China plain, Atmos. Chem. Phys., 11, 3479–3494,

819   https://doi.org/10.5194/acp-11-3479-2011, 2011.

820   Lu, Y., Yan, C., Fu, Y., Chen, Y., Liu, Y., Yang, G., Wang, Y., Bianchi, F., Chu, B.,

821   Zhou, Y., Yin, R., Baalbaki, R., Garmash, O., Deng, C., Wang, W., Liu, Y., Petäjä, T.,

822   Kerminen, V. M., Jiang, J., Kulmala, M., and Wang, L.: A proxy for atmospheric

823   daytime gaseous sulfuric acid concentration in urban Beijing, Atmos. Chem. Phys., 19,

824   1971–1983, https://doi.org/10.5194/acp-19-1971-2019, 2019.

825   Luoma, K., Virkkula, A., Aalto, P., Petäjä, T., and Kulmala, M.: Over a 10-year record

826   of aerosol optical properties at SMEAR II, Atmos. Chem. Phys., 19, 11363–11382,

827   https://doi.org/10.5194/acp-19-11363-2019, 2019.

828   Ma, C. Sen, Ma, G., and Pincebourde, S.: Survive a Warming Climate: Insect

829   Responses to Extreme High Temperatures, Annu. Rev. Entomol., 66, 163–184,

830   https://doi.org/10.1146/annurev-ento-041520-074454, 2021.

831   Ma, N., Zhao, C., Tao, J., Wu, Z., Kecorius, S., Wang, Z., Groß, J., Liu, H., Bian, Y.,

832   Kuang, Y., Teich, M., Spindler, G., Muller, K., Van Pinxteren, D., Herrmann, H., Hu,

833   M., and Wiedensohler, A.: Variation of CCN activity during new particle formation

834   events in the North China Plain, Atmos. Chem. Phys., 16, 8593–8607,

835   https://doi.org/10.5194/acp-16-8593-2016, 2016.

836   Mishchenko, M. I.: Electromagnetic scattering by nonspherical particles: A tutorial

837   review, J. Quant. Spectrosc. Radiat. Transf., 110, 808–832,

838   https://doi.org/10.1016/j.jqsrt.2008.12.005, 2009.

839   Petters, M. D. and Kreidenweis, S. M.: A single parameter representation of

840   hygroscopic growth and cloud condensation nucleus activity, Atmos. Chem. Phys., 7,

841   1961–1971, https://doi.org/10.5194/acp-7-1961-2007, 2007.

842   Pierce, T. E. and Waldruff, P. S.: Pc-beis: A personal computer version of the biogenic

843   emissions inventory system, J. Air Waste Manag. Assoc., 41, 937–941,

844   https://doi.org/10.1080/10473289.1991.10466890, 1991.

845   Qi, X. M., Ding, A. J., Nie, W., Petäjä, T., Kerminen, V. M., Herrmann, E., Xie, Y. N.,

846   Zheng, L. F., Manninen, H., Aalto, P., Sun, J. N., Xu, Z. N., Chi, X. G., Huang, X.,

847   Boy, M., Virkkula, A., Yang, X. Q., Fu, C. B., and Kulmala, M.: Aerosol size

848   distribution and new particle formation in the western Yangtze River Delta of China:

849   2 years of measurements at the SORPES station, Atmos. Chem. Phys., 15,

850   12445–12464, https://doi.org/10.5194/acp-15-12445-2015, 2015.

851   Quinn, P. K., Bates, T. S., Baynard, T., Clarke, A. D., Onasch, T. B., Wang, W., Rood,

852   M. J., Andrews, E., Allan, J., Carrico, C. M., Coffman, D., and Worsnop, D.: Impact

853   of particulate organic matter on the relative humidity dependence of light scattering: A

854   simplified   parameterization,   Geophys.   Res.   Lett.,   32,   1–4,

855   https://doi.org/10.1029/2005GL024322, 2005.

856   Ren, J., Chen, L., Fan, T., Liu, J., Jiang, S., and Zhang, F.: The NPF Effect on CCN

857   Number Concentrations: A Review and Re-Evaluation of Observations From 35 Sites

858   Worldwide, Geophys. Res. Lett., 48, 1–12, https://doi.org/10.1029/2021GL095190,

859   2021.

860   Salma, I., Thén, W., Aalto, P., Kerminen, V. M., Kern, A., Barcza, Z., Petäjä, T., and

861   Kulmala, M.: Influence of vegetation on occurrence and time distributions of regional

862   new aerosol particle formation and growth, Atmos. Chem. Phys., 21, 2861–2880,

863   https://doi.org/10.5194/acp-21-2861-2021, 2021.

864 Schuster, G. L., Dubovik, O., and Holben, B. N.: Angstrom exponent and bimodal

865 aerosol size distributions, J. Geophys. Res. Atmos., 111, 1–14,

866 https://doi.org/10.1029/2005JD006328, 2006.

867 Sharma, S. and Mujumdar, P.: Increasing frequency and spatial extent of concurrent

868 meteorological droughts and heatwaves in India, Sci. Rep., 7, 1–9,

869 https://doi.org/10.1038/s41598-017-15896-3, 2017.

870 Su, Y. W.: The effects of extreme high temperature day off on electricity conservation,

871 Weather. Clim. Soc., 13, 769–782, https://doi.org/10.1175/WCAS-D-20-0176.1, 2021.

872 Sun, J., Hermann, M., Weinhold, K., Merkel, M., Birmili, W., Yang, Y., Flentje, H.,

873 Ries, L., Couret, C., Elsasser, M., Sohmer, R., Wirtz, K., Meinhardt, F., Schü, M.,

874 Bath, O., Hellack, B., Kerminen, V., Kulmala, M., Ma, N., and Wiedensohler, A.:

875 Measurement report : Contribution of atmospheric new particle formation to ultrafine

876 particle concentration , cloud condensation nuclei and radiative forcing : Results from

877 five-year observations in Central Europe, Atmos. Chem. Phys., 1–34, 2024.

878 Sun, Y., Song, L., Yin, H., Zhang, X., Stott, P., Zhou, B., and Hu, T.: 20. Human

879 influence on the 2015 extreme high temperature events in Western China, Bull. Am.

880 Meteorol. Soc., 97, S102–S106, https://doi.org/10.1175/BAMS-D-16-0158.1, 2016.

881 Tang, M., Chan, C. K., Li, Y. J., Su, H., Ma, Q., Wu, Z., Zhang, G., Wang, Z., Ge, M.,

882 Hu, M., He, H., and Wang, X.: A review of experimental techniques for aerosol

883 hygroscopicity studies, Atmos. Chem. Phys., 19, 12631–12686,

884 https://doi.org/10.5194/acp-19-12631-2019, 2019.

885 Tao, L., Zhou, Z., Tao, J., Zhang, L., Wu, C., Li, J., Yue, D., Wu, Z., Zhang, Z., Yuan,

886 Z., Huang, J., and Wang, B.: High contribution of new particle formation to ultrafine

887 particles in four seasons in an urban atmosphere in south China, Sci. Total Environ.,

888 889, https://doi.org/10.1016/j.scitotenv.2023.164202, 2023.

889   Teng, M., Liao, H., Burke, P. J., Chen, T., and Zhang, C.: Adaptive responses: the
890   effects of temperature levels on residential electricity use in China, Clim. Change, 172,
891   https://doi.org/10.1007/s10584-022-03374-3, 2022.

892   Tian, J., Wang, Q., Zhang, Y., Yan, M., Liu, H., Zhang, N., Ran, W., and Cao, J.:
893   Impacts of primary emissions and secondary aerosol formation on air pollution in an
894   urban area of China during the COVID-19 lockdown, Environ. Int., 150, 106426,
895   https://doi.org/10.1016/j.envint.2021.106426, 2021.

896   Titos, G., Burgos, M. A., Zieger, P., Alados-Arboledas, L., Baltensperger, U.,
897   Jefferson, A., Sherman, J., Weingartner, E., Henzing, B., Luoma, K., O'Dowd, C.,
898   Wiedensohler, A., and Andrews, E.: A global study of hygroscopicity-driven
899   light-scattering enhancement in the context of other in situ aerosol optical properties,
900   Atmos. Chem. Phys., 21, 13031–13050, https://doi.org/10.5194/acp-21-13031-2021,
901   2021.

902   Titos, G., Cazorla, A., Zieger, P., Andrews, E., Lyamani, H., Granados-Muñoz, M. J.,
903   Olmo, F. J., and Alados-Arboledas, L.: Effect of hygroscopic growth on the aerosol
904   light-scattering coefficient: A review of measurements, techniques and error sources,
905   Atmos. Environ., 141, 494–507, https://doi.org/10.1016/j.atmosenv.2016.07.021,
906   2016.

907   Titos, G., Lyamani, H., Cazorla, A., Sorribas, M., Foyo-Moreno, I., Wiedensohler, A.,
908   and Alados-Arboledas, L.: Study of the relative humidity dependence of aerosol
909   light-scattering in southern Spain, Tellus, Ser. B Chem. Phys. Meteorol., 66,
910   https://doi.org/10.3402/tellusb.v66.24536, 2014.

911   Wang, Y., Li, Z., Zhang, R., Jin, X., Xu, W., Fan, X., Wu, H., Zhang, F., Sun, Y., Wang,
912   Q., Cribb, M., and Hu, D.: Distinct Ultrafine- and Accumulation-Mode Particle
913   Properties in Clean and Polluted Urban Environments, Geophys. Res. Lett., 46,
914   10918–10925, https://doi.org/10.1029/2019GL084047, 2019.

915 Wang, Z. B., Hu, M., Sun, J. Y., Wu, Z. J., Yue, D. L., Shen, X. J., Zhang, Y. M., Pei,
916 X. Y., Cheng, Y. F., and Wiedensohler, A.: Characteristics of regional new particle
917 formation in urban and regional background environments in the North China Plain,
918 Atmos. Chem. Phys., 13, 12495–12506, https://doi.org/10.5194/acp-13-12495-2013,
919 2013.

920 Wang, Z., Wu, Z., Yue, D., Shang, D., Guo, S., Sun, J., Ding, A., Wang, L., Jiang, J.,
921 Guo, H., Gao, J., Cheung, H. C., Morawska, L., Keywood, M., and Hu, M.: New
922 particle formation in China: Current knowledge and further directions, Sci. Total
923 Environ., 577, 258–266, https://doi.org/10.1016/j.scitotenv.2016.10.177, 2017.

924 Wu, Z. J., Poulain, L., Birmili, W., Größ, J., Niedermeier, N., Wang, Z. B., Herrmann,
925 H., and Wiedensohler, A.: Some insights into the condensing vapors driving new
926 particle growth to CCN sizes on the basis of hygroscopicity measurements, Atmos.
927 Chem. Phys., 15, 13071–13083, https://doi.org/10.5194/acp-15-13071-2015, 2015.

928 Wu, Z. J., Zheng, J., Shang, D. J., Du, Z. F., Wu, Y. S., Zeng, L. M., Wiedensohler, A.,
929 and Hu, M.: Particle hygroscopicity and its link to chemical composition in the urban
930 atmosphere of Beijing, China, during summertime, Atmos. Chem. Phys., 16,
931 1123–1138, https://doi.org/10.5194/acp-16-1123-2016, 2016.

932 Xia, C., Sun, J., Hu, X., Shen, X., Zhang, Y., Zhang, S., Wang, J., Liu, Q., Lu, J., Liu,
933 S., and Zhang, X.: Effects of hygroscopicity on aerosol optical properties and direct
934 radiative forcing in Beijing: Based on two-year observations, Sci. Total Environ., 857,
935 159233, https://doi.org/10.1016/j.scitotenv.2022.159233, 2023.

936 Xu, W. Y., Zhao, C. S., Ran, L., Deng, Z. Z., Liu, P. F., Ma, N., Lin, W. L., Xu, X. B.,
937 Yan, P., He, X., Yu, J., Liang, W. D., and Chen, L. L.: Characteristics of pollutants and
938 their correlation to meteorological conditions at a suburban site in the North China
939 Plain, Atmos. Chem. Phys., 11, 4353–4369, https://doi.org/10.5194/acp-11-4353-2011,
940 2011.

941   Xue, B., Kuang, Y., Xu, W., and Zhao, P.: Joint increase of aerosol scattering

942   efficiency and aerosol hygroscopicity aggravate visibility impairment in the North

943   China   Plain,   Sci.   Total   Environ.,   839,   141163,

944   https://doi.org/10.1016/j.scitotenv.2022.156279, 2022.

945   Yang, P., Feng, Q., Hong, G., Kattawar, G. W., Wiscombe, W. J., Mishchenko, M. I.,

946   Dubovik, O., Laszlo, I., and Sokolik, I. N.: Modeling of the scattering and radiative

947   properties of nonspherical dust-like aerosols, J. Aerosol Sci., 38, 995–1014,

948   https://doi.org/10.1016/j.jaerosci.2007.07.001, 2007.

949   Yarragunta, Y., Srivastava, S., Mitra, D., and Chandola, H. C.: Source apportionment

950   of carbon monoxide over India: a quantitative analysis using MOZART-4, Environ.

951   Sci. Pollut. Res., 28, 8722–8742, https://doi.org/10.1007/s11356-020-11099-y, 2021.

952   Zhang, L., Sun, J. Y., Shen, X. J., Zhang, Y. M., Che, H., Ma, Q. L., Zhang, Y. W.,

953   Zhang, X. Y., and Ogren, J. A.: Observations of relative humidity effects on aerosol

954   light scattering in the Yangtze River Delta of China, Atmos. Chem. Phys., 15,

955   8439–8454, https://doi.org/10.5194/acp-15-8439-2015, 2015.

956   Zhang, R., Khalizov, A. F., Pagels, J., Zhang, D., Xue, H., and McMurry, P. H.:

957   Variability in morphology, hygroscopicity, and optical properties of soot aerosols

958   during atmospheric processing, Proc. Natl. Acad. Sci. U. S. A., 105, 10291–10296,

959   https://doi.org/10.1073/pnas.0804860105, 2008.

960   Zhang, R., Khalizov, A., Wang, L., Hu, M., and Xu, W.: Nucleation and growth of

961   nanoparticles   in   the   atmosphere,   Chem.   Rev.,   112,   1957–2011,

962   https://doi.org/10.1021/cr2001756, 2012.

963   Zhang, R., Suh, I., Zhao, J., Zhang, D., Fortner, E. C., Tie, X., Molina, L. T., and

964   Molina, M. J.: Atmospheric new particle formation enhanced by organic acids,

965   Science (80-.)., 304, 1487–1490, https://doi.org/10.1126/science.1095139, 2004.

966   Zhang, R., Wang, G., Guo, S., Zamora, M. L., Ying, Q., Lin, Y., Wang, W., Hu, M.,

967   and Wang, Y.: Formation of Urban Fine Particulate Matter, Chem. Rev., 115,

968   3803–3855, https://doi.org/10.1021/acs.chemrev.5b00067, 2015.

969   Zhang, Z., Xu, W., Zeng, S., Liu, Y., Liu, T., Zhang, Y., Du, A., Li, Y., Zhang, N.,

970   Wang, J., Aruffo, E., Han, P., Li, J., Wang, Z., and Sun, Y.: Secondary Organic

971   Aerosol Formation from Ambient Air in Summer in Urban Beijing: Contribution of

972   S/IVOCs and Impacts of Heat Waves, Environ. Sci. Technol. Lett.,

973   https://doi.org/10.1021/acs.estlett.4c00415, 2024.

974   Zhao, C., Yu, Y., Kuang, Y., Tao, J., and Zhao, G.: Recent Progress of Aerosol

975   Light-scattering Enhancement Factor Studies in China, Adv. Atmos. Sci., 36,

976   1015–1026, https://doi.org/10.1007/s00376-019-8248-1, 2019.

977   Zhao, S., Yu, Y., Li, J., Yin, D., Qi, S., and Qin, D.: Response of particle number

978   concentrations to the clean air action plan: Lessons from the first long-term aerosol

979   measurements in a typical urban valley in western China, Atmos. Chem. Phys., 21,

980   14959–14981, https://doi.org/10.5194/acp-21-14959-2021, 2021.

981   Zhu, Y., Shen, Y., Li, K., Meng, H., Sun, Y., Yao, X., Gao, H., Xue, L., and Wang, W.:

982   Investigation of Particle Number Concentrations and New Particle Formation With

983   Largely Reduced Air Pollutant Emissions at a Coastal Semi-Urban Site in Northern

984   China, J. Geophys. Res. Atmos., 126, 1–20, https://doi.org/10.1029/2021JD035419,

985   2021.

986   Zieger, P., Weingartner, E., Henzing, J., Moerman, M., De Leeuw, G., Mikkilä, J., Ehn,

987   M., Petäjä, T., Clémer, K., Van Roozendael, M., Yilmaz, S., Frieß, U., Irie, H., Wagner,

988   T., Shaiganfar, R., Beirle, S., Apituley, A., Wilson, K., and Baltensperger, U.:

989   Comparison of ambient aerosol extinction coefficients obtained from in-situ,

990   MAX-DOAS and LIDAR measurements at Cabauw, Atmos. Chem. Phys., 11,

991   2603–2624, https://doi.org/10.5194/acp-11-2603-2011, 2011.